Chinese Chemical Letters 33 (2022) 3161–3166

Contents lists available at ScienceDirect

Chinese Chemical Letters

journal homepage: www.elsevier.com/locate/cclet

Self-doped Br in Bi_5O_7Br ultrathin nanotubes: Efficient photocatalytic NO purification and mechanism investigation

Ping Yan[a,b], Qin Ren[b], Fengyi Zhong[b], Jieyuan Li[b], Fusheng Wei[a], Jianjun Li[a,*], Xian Shi[b,*], Fan Dong[b,c]

[a] College of Architecture and Environment, Sichuan University, Chengdu 610065, China
[b] Yangtze Delta Region Institute (Huzhou) & Institute of Fundamental and Frontier Sciences, University of Electronic Science and Technology of China, Huzhou 313001, China
[c] State Centre for International Cooperation on Designer Low carbon and Environmental Materials (CDLCEM), School of Materials Science and Engineering, Zhengzhou University, Zhengzhou 450001, China

ARTICLE INFO

Article history:
Received 28 June 2021
Revised 17 September 2021
Accepted 27 October 2021
Available online 2 November 2021

Keywords:
Bi_5O_7Br
Br auto-doped
Photocatalytic no removal
DFT
In situ DRIFT

ABSTRACT

Bismuth-rich Bi_5O_7Br is a promising photocatalyst for pollutant removal owing to its stability and appropriate band structure in comparison with bismuth oxybromide. However, bulk-phase Bi_5O_7Br suffers from poor light absorption and high charge recombination rates resulting in poor activity. Elemental doping is a powerful strategy to enhance photocatalytic activity. In this study, we prepared a series of Br auto-doped ultrathin Bi_5O_7Br nanotubes and explored the effect of Br doping on photocatalytic NO removal. The optimal doping content was determined *via* a photocatalytic NO removal experiment, which revealed the optimal ratio of Bi and Br was approximately 3:1. *In situ* diffuse reflectance infrared Fourier transform spectroscopy (*In situ* DRIFT) and density functional theory (DFT) studies revealed that NO removal mechanism catalyzed by Br doped Bi_5O_7Br. Our work presents a new strategy for the enhancement of photocatalytic pollutant degradation by bismuth oxyhalide photocatalysts.

The concentration of atmospheric nitric oxide (NO) is continually increasing, due to the increase in industrial activities and transportation [1–3]. Numerous measures need to be taken to remove NO, since NO is harmful to human health and contributes to the global air pollution problem [4]. In recent years, photocatalytic technology has been regarded as a promising and attractive technology to control atmospheric NO pollution [5–8]. Ideal catalysts for photocatalytic removal are highly active towards molecular oxygen and are activated under visible light, however active catalysts are elusive to discover with many possessing poor carrier separation efficiencies.

Various photocatalysts have been studied for photocatalytic NO removal and significant advancements have been made [9–11]. Among these, visible-light responsive bismuth oxyhalide semiconductors with special layered structures have attracted a wide range of interest and have been considered as one of the most promising photocatalysts for NO removal [12–14]. It has been found that by changing the ratio of bismuth (Bi), oxygen (O), and halogen (Cl, Br and I), this can induce anisotropic p states or hybrid sp states and simultaneously lead to a highly dispersed conduction band (CB) and valence band (VB). Greater charge transfer under photoexcitation is known to be critical in photocatalytic NO degradation. The present research focus has moved away from bulk phase BiOX (X = Br, Cl and I) catalysts and has moved towards preparing more active bismuth rich photocatalytic materials ($Bi_xO_yX_z$, x:y:z ≠ 1:1:1, X = Br, Cl and I). These include, Bi_3O_4Br [15], $Bi_{24}O_{31}Cl_{10}$ [16], Bi_5O_7X (X = Cl, Br, I) [17], $Bi_4O_5I_2$ [18] and so on. For example, Bi_5O_7Br displays excellent activity towards nitrogen fixation, pollutant degradation and H_2 evolution [19–21]. However, the photocatalytic properties are still greatly limited by the intrinsically high recombination rate of photo-generated charge carriers and poor light absorption.

To improve the photocatalytic properties of Bi_5O_7Br, many strategies, such as defect engineering [22], doping with metals and non-metals, surface functionalization, metal deposition, and combination with semiconductor catalysts have been investigated [23–26]. Varying the morphology has also been investigated and various forms of nanostructures [27], such as nanotubes, nanoparticles, and nanosheets have been prepared to shorten the carrier diffusion length and improve electron transport [28–30]. Meanwhile, self-doping has been regarded as an effective approach to boost

* Corresponding authors.
E-mail addresses: jjli@scu.edu.cn (J. Li), shixian930501@163.com (X. Shi).

https://doi.org/10.1016/j.cclet.2021.10.082
1001-8417/

the photocatalytic performance of catalysts as it enables control of the number of active sites. Furthermore, it permits tuning of the electronic and band structures without introducing extraneous elements and thus avoids the destruction of the pristine configuration [31,32]. For example, Wang *et al.* [33] reported that Sn self-doped $CaSn(OH)_6$ could optimize the local electron structure, increasing the rate of activation and oxidation of important intermediate products (HCOOH). This leaded to a suppression in the generation of toxic products, and presents a safe and efficient approach to photocatalytically remove formaldehyde. Using theoretical and experimental means, Zhang's group [34] found Bi self-doping Bi_2WO_6 enhances the charge separation and transfer to improve the photocatalytic degradation of sodium pentachlorophenate. However, there is no formula to predict the effect of self-doping on the photocatalytic properties of Bi_5O_7Br, and the promotion mechanism has not been fully determined. Accordingly, the activation mechanism for improved photocatalytic performance on self-doping Bi_5O_7Br requires further investigation in order to rationally design highly active photocatalysts.

In this study, a series of Bi_5O_7Br nanostructures were obtained *via* the facile precipitation method by controlling the amount of KBr. Among the series, Bi_5O_7Br-40 displayed the best performance towards NO photoremoval, and had the largest specific surface area (153.6 m^2/g) and the best optical absorption property among those evaluated. Density functional theory (DFT) calculations revealed that introducing Br self-doping can reduce the bandgap of Bi_5O_7Br and tune the band position to improve the oxidation properties of the catalyst. NO adsorption, electronic transfer, and local electron structures are all significantly increased by Br doping. The experimental results show that more superoxide radicals are produced by Br-40 resulting in outstanding efficiency towards photocatalytic NO removal during visible light illumination. To explore the photocatalytic mechanism of NO removal, *in situ* DRIFT was used to monitor the adsorption and photocatalytic processes, and the intermediate products formed, and the conversion of NO over time. We have demonstrated a new approach to increase the charge separation and improve the photocatalytic activity of bismuth oxyhalide photocatalysts under visible light irradiation.

Bi_5O_7Br nanotubes were prepared *via* a facile room-temperature precipitation method. 0.25 g of $Bi(NO_3)_3{\cdot}5H_2O$ was mixed in 20 mL of EG at room temperature with continuous magnetic stirring. After complete dissolution, 15 mL of oleylamine was added followed by 15 mL of ethanol. KBr solid (0.01, 0.02, 0.04 and 0.06 g) was added and the resultant mixture was stirred for 30 min. 20 mL of deionized water then added into the mixture, which was then stirred for 24 h, after which a solution was obtained. The aqueous phase was washed with *n*-heptane and ethanol several times, and then was dried at 60 °C. This furnished were tagged as either Br-10, Br-20, Br-40, or Br-60. The performances of the reagents and characterization instrument information of the sample are shown in the Supporting information.

Photocatalytic properties were assessed by determining the removal ratio of NO at 500 ppb in a continuous-flow reactor, which measured 30 cm × 15 cm × 10 cm (long × wide × high). A 150 W commercial tungsten halogen lamp was vertically set outside the reactor which was turned on after achieving an adsorption-desorption equilibrium. Removing the UV light in the light beam by accomplished by a UV cutoff filter (420 nm). The as-prepared sample (0.20 g) was dispersed and coated onto two glass dishes (12.0 cm in diameter) for photocatalytic activity tests. The concentration of NO was continuously measured by a NO_x analyser (Thermo Environmental Instruments Inc., model 42i-TL). The removal ratio (η) of NO was defined as (Eq. 1):

$$\eta(\%) = (1 - C/C_0) \times 100\% \quad (1)$$

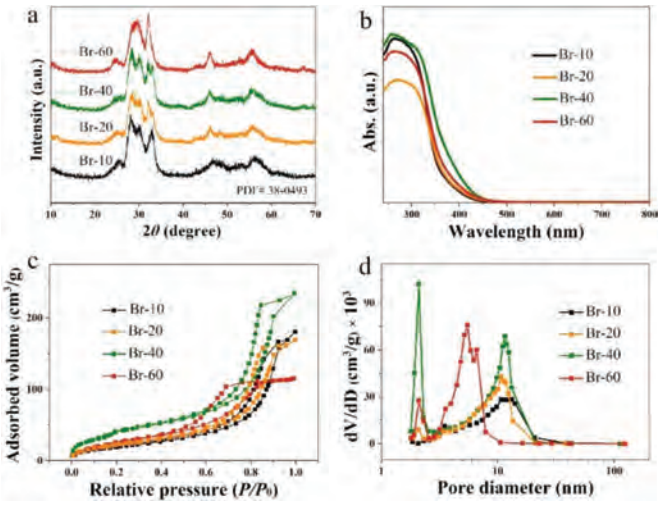

Fig. 1. (a) XRD patterns of Br-10, Br-20, Br-40 and Br-60. (b) UV–vis diffuse reflectance spectra of the prepared samples. (c) N_2 adsorption-desorption isotherms and (d) pore-size distribution curves of different samples.

where C and C_0 are concentrations of NO in the outlet stream and feeding stream, respectively.

The *in situ* diffuse reflectance infrared Fourier transform spectroscopy (DRIFTS) measurements were conducted in a high-temperature reaction chamber and recorded on a Tensor II FTIR spectrometer (Bruker) equipped with an *in situ* diffuse reflectance cell (Harrick). The photocatalysts were placed into an Ar gas filled (50 mL/min) reaction chamber at 110 °C to clear the residual hydrocarbon, H_2O, and CO_2 after heat treatment and the real-time FT-IR spectrum was recorded as the background. Then, the reaction gas (50 mL/min NO, 50 mL/min O_2) was transferred into the reaction chamber. NO adsorption onto the photocatalysts was conducted for 20 min, before the photocatalysts were illuminated under visible light for 50 min. During the process of adsorption and the first thirty minutes of the reaction, IR spectra were recorded every 2 min, and afterwards were recorded every 10 min. The IR scanning range was 600–4000 cm^{-1} in order to elucidate the photocatalytic oxidation process.

Density functional theory (DFT) calculations were performed by employing the VASP5.4 code [35,36], using the generalized gradient approximation with the Perdew–Burke–Ernzerhof (PBE) exchange and correlation functional [37]. A plane-wave basis set with cut-off energy of 400 eV within the framework of the projector-augmented wave (PAW) method was carried out [38,39], along with a $3 \times 3 \times 1$ Monkhorst Pack grid for the Brillouin zone. The Gaussian smearing width was set to 0.2 eV. The van der Waals (vdW) correction was described by the D2 method of Grimme. All atoms were afforded to relax and converge to 0.01 eV/Å in all systems. A 156 atom $2 \times 3 \times 1$ supercell of Bi_5O_7Br (571Br) was relaxed, then Br self-doping was introduced, which is shown in Fig. S1 (Supporting information).

The adsorption energy (ΔE_{ad}) is defined as Eq. 2:

$$\Delta E_{ad} = E_{tot} - (E_s + E_m) \quad (2)$$

where E_{tot}, E_s and E_m are the total energy of the adsorption complex, the 571Br material, and the isolated molecule, respectively.

XRD patterns of the prepared samples were recorded to identify their crystal structures. As shown in Fig. 1a, the XRD patterns of Br-10, Br-20, Br-40 and Br-60 could be properly indexed to the phase of Bi_5O_7Br (JCPDS No. 38–0493). The diffraction peaks of the Br-10, Br-20, Br-40, Br-60 samples at 2θ were 28.29°, 31.07° and 33.39° consistent with the (312), (004) and (600) of Bi_5O_7Br, respectively. It is observed in Fig. S2 (Supporting information), the

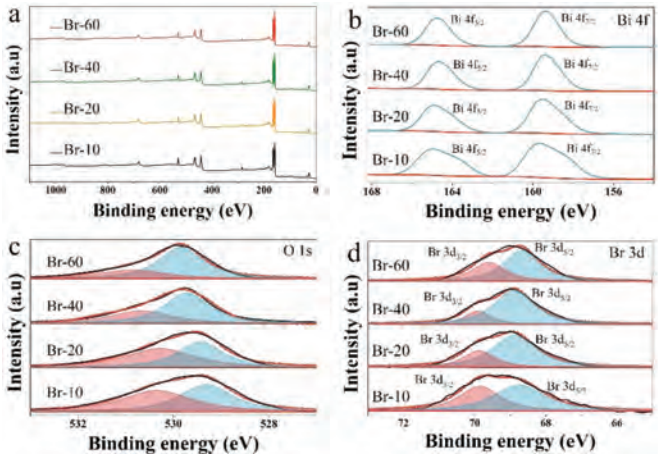

Fig. 2. XPS spectra and elemental content table of the samples, (a) full scan, (b) Bi 4f, (c) O 1s, (d) Br 3d.

peaks gradually shifted to a lower angle with increasing levels of the starting material KBr, and the crystallinity started to deteriorate when 0.06 g of KBr was added (Br-60). Furthermore, the optical absorption properties of the samples were revealed through UV–vis diffuse reflectance spectroscopy. It was found that the absorption spectra of the samples showed a red shift from pristine Br-10, with Br-40 possessing the optimal absorbance (Fig. 1b). The band gaps (Fig. S3 in Supporting information) were measured as 3.16 eV, 2.72 eV, 2.57 eV and 2.63 eV for Br-10, Br-20, Br-40 and Br-60, respectively. This indicates the optical absorption maxima of the samples ranged from ultraviolet absorption through to visible light adsorption wavelengths, whilst the visible light adsorption performance was improved with increased Br doping.

As can be seen in Figs. 1c and d, the BET expressed specific surface area and the pore structure of the samples was investigated. According to the Brunauer-Deming-Deming-Teller (BDDT) classification, the prepared samples were all type IV adsorption isotherms, indicating the existence of mesopores in the structures. Table S1 (Supporting information) shows the specific surface areas and the pore volumes of the samples. The specific surface areas were calculated as 73.0 m^2/g for Br-10, 83.3 m^2/g for Br-20, 153.6 m^2/g for Br-40, and 101.2 m^2/g for Br-60. Br-40 had the largest surface area among the synthesized samples evaluated, which indicates it may possess a higher adsorption performance for NO compared with the other materials. Additionally, the pore volumes of the samples were between 0.210 cm^3/g and 0.398 cm^3/g, of which Br-40 had the largest pore volume.

The detailed elemental composition of the prepared Br-10, Br-20, Br-40, and Br-60 samples was investigated by XPS spectroscopy. As shown in Fig. 2a, Bi, O, C and Br on the surface of the samples were indexed in the survey scan spectra. Two bands at about 164.9 eV and 159.7 eV in Fig. 2b correspond to Bi $4f_{5/2}$ and Bi $4f_{7/2}$, respectively. This verifies that Bi is in the trivalent state [40]. Fig. 2c shows that the binding energies for O 1s are 530.3 eV and 529.3 eV and correspond to the Bi−O bond in Bi_5O_7Br and the adsorption of oxygen-containing species (H_2O and −OH) on Bi_5O_7Br [41,42]. The peaks for Br 3d at approximately 69.9 eV and 68.7 eV correspond to Br $3d_{3/2}$ and $3d_{5/2}$, respectively (Fig. 2d). Moreover, the elemental content of Bi and Br in the samples and their ratio was assessed by XPS (Table 1). The ratio of Bi and Br for Br-10 was estimated at approximately 5:1 in pristine Bi_5O_7Br. The ratio between Bi and Br was shown by XPS to gradually decrease with increasing amounts of KBr. This increase in Br is known as self-doping, and the doping concentration is increasing from Br-20 to Br-60.

Table 1
Content and ratio of elements for Br-10, Br-20, Br-40 and Br-60.

Name	Bi 4f	Br 3d	Bi/Br
Br-10	16.12	3.38	4.78:1
Br-20	20.35	6.39	3.18:1
Br-40	20.31	7.87	2.58:1
Br-60	21.09	8.90	2.37:1

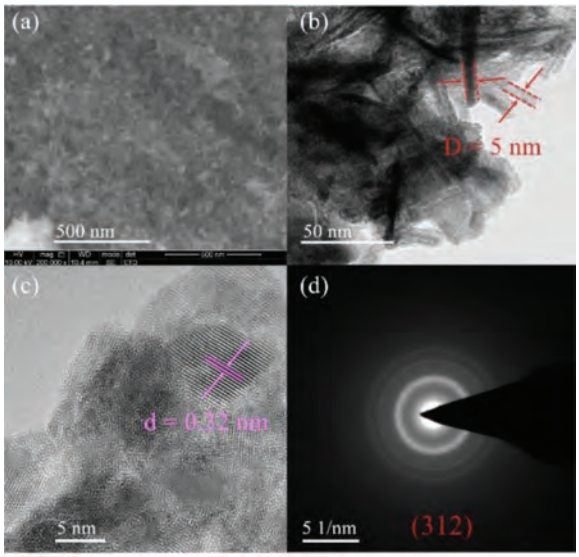

Fig. 3. SEM image of Br-40 (a), HR-TEM patterns of Br-40 (b, c). Electron diffraction image of Br-40 (d).

The morphology and structure of the prepared samples were characterized by SEM and HR-TEM. The SEM images of the Br-10, Br-20, Br-60, and Br-40 samples is shown in Figs. S3a-c (Supporting information) and Fig. 3a. The samples exhibit a cotton-like shape comprised of small cotton tubes. HR-TEM was carried out to determine the micromorphology of the prepared samples and is shown in Fig. 3 and Fig. S4 (Supporting information). HR-TEM revealed the water-assisted atomic self-assembly with a small quantity of KBr leads to the formation of nanotube structures. The size of the nanotubes formed varied with the amount of KBr present. Of the samples evaluated, the Br-40 sample possessed the largest tube diameter. As shown in Figs. 3b and c, the cross-sectional diameter of the nanotubes in the Br-40 sample was *ca.* 5 nm (red border) and the lattice fringes had an interplanar spacing of 0.32 nm (purple border). These were confirmed as (312) crystalline facets, corresponding to the patterns of the selected-area electron diffraction (Fig. 3d) [28]. The Br-40 sample possesses the largest specific surface area, pore volume, and nanotube diameter. The EDS of the Br-10 and Br-40 samples were analyzed to further verify the elemental content. As demonstrated in Fig. S5 (Supporting information), the elemental ratio for Br and Bi in Br-10 and Br-40 is 5:1 and 3:1, respectively. This is consistent with the XPS data, indicating Br self-doping with increasing levels of KBr.

Furthermore, DFT was employed to confirm whether Br self-doping could improve photocatalytic NO removal and the band structure of Br self-doped Bi_5O_7Br (Br-571Br) compared to 571Br. The total density of state (TDOS) of 571 Br and Br-571Br and the partial density of state (PDOS) for the Bi atom in the two materials was examined to explore the influence of introducing Br self-doping in Bi_5O_7Br. As shown in Fig. 4a, Br self-doping generates a peak at the bottom of the conduction band leading to a reduction the bandgap from 2.37 eV to 1.85 eV. Meanwhile, the TDOS peak for Br-571Br shifts to the left, indicating an improvement in the oxida-

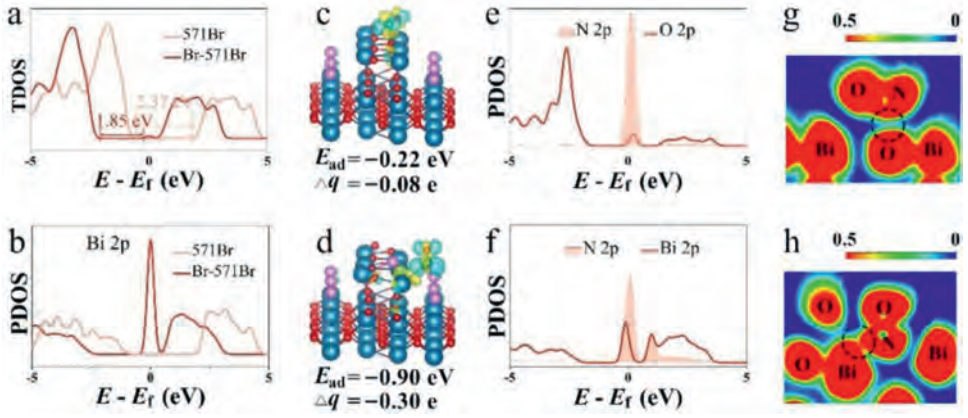

Fig. 4. The TDOS of 571Br and Br-571Br (a). PDOS of Bi for 571Br and Br-571Br (b). The Fermi level is set to 0 eV. The charge density difference and Bader values of adsorbed NO for 571Br (c) and Br-571Br (d). The isosurfaces are 0.01 eV/Å^3. Δq represents the sum of the charge transfer numbers of the adsorbed NO. The Bader value is in e; The ELF for 571Br (e) and Br-571Br (f). The partial density of state (PDOS) of adsorbed NO on 571Br (g) and Br-571Br (h), respectively.

tion performance. Accordingly, Br self-doping in Bi_5O_7Br appears favorable for NO removal by oxidation. Furthermore, the PDOS of Bi 2p in Br-571Br had a distinct peak at the bottom of the conduction band around the Fermi level, which serves the TDOS (Fig. 4b). This indicates the introduction of Br self-doping may enable the tailoring of the density of state for the Bi atom adjacent to the doped Br atom, to improve the band structure of Bi_5O_7Br, facilitating catalytic NO removal.

To explore the effect of Br self-doping on NO removal, the adsorption properties and electronic structure of NO adsorbed onto the 571Br and Br-571Br were studied. As showed in Figs. 4c and d, NO preferentially adsorbs onto Br-571Br over 571Br. The adsorption energy for Br-571Br is −0.90 eV while that for 571Br is −0.22 eV. Besides, the adsorption site was on the O atom for 571Br which was altered by the adjacent Bi atom doped with Br. Charge density difference and Bader analysis revealed NO adsorbed on Br-571Br has a large electron density indicated by the Bader value of −0.30 e. On the contrary, the Bader value of NO adsorbed on 571Br is −0.08 e. It is found that both the NO adsorption energy and the rate of electron transfer for Br-571Br is more than three times that of 571Br. PDOS and the electron local function (ELF) were assessed to reveal the interaction between the adsorbed NO and the photocatalyst. As shown in Figs. 4e and f, the peaks corresponding to N 2p (the N atom of adsorbed NO) on Br-571Br more overlapped with the peaks corresponding to Bi 2p (the Bi atom of Bi5O7Br) compared with those for 571Br. This indicates that the interaction between NO and Br-571Br is stronger. The boundary between the N atom of adsorbed NO and the Bi surface atom of Br-571Br is almost red (see the black circle, Figs. 4g and h), while it is almost observed blue between the N atom and the O atom of 571Br (Figs. 4g and h). This indicates adsorbed NO intensively interacts with the surface of the Br-571Br material. Fig. S6 (Supporting information) reveals that the interaction between NO and 571Br is weaker than that between NO and Br-571Br because of the covalent action values of 11% for 571Br and 36% for Br-571Br.

Br self-doping in Bi_5O_7Br appears to enhance NO removal by increasing the adsorption of NO, accelerating the charge transfer between NO and the photocatalyst surface, and strengthening the interaction between NO and Bi_5O_7Br materials.

Additionally, we experimentally investigated the photocatalytic properties of the prepared Br self-doping samples towards NO degradation under visible light irradiation. The NO removal rate for Br self-doping is shown in Fig. 5a, and reveals Br-40 has the highest activity (Br-10 (26%) < Br-20 (35%) < Br-40 (44%) > Br-60 (33%)). Br-40 was then further studied in a cycle test to examine the stability and durability of the catalyst towards NO removal

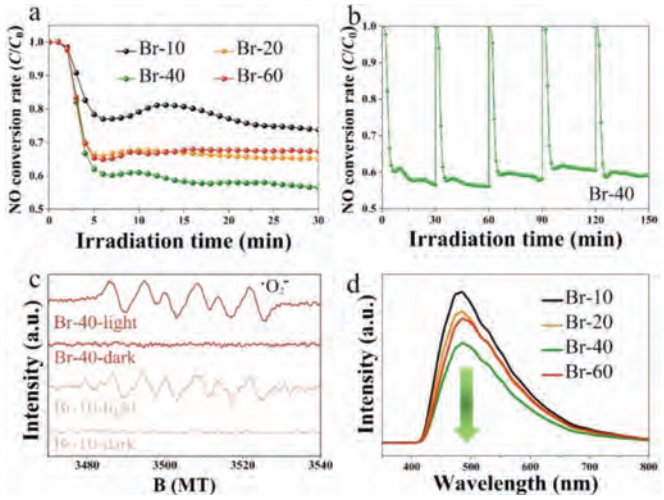

Fig. 5. (a) Photocatalytic activity of NO degradation under visible light. (b) The cycling test of Br-40 under visible irradiation. (c) ESR spectra of superoxide radicals generated from Br-10 and Br-40; (d) PL spectrum of Br-10, Br-20, Br-40 and Br-60.

(Fig. 5b). The NO removal performance slightly decreased but leveled out to approximately 41% after the five cycles, indicating good catalyst stability.

Br-40 exhibits excellent activity for NO degradation, and the difference in activity compared with undoped Bi_5O_7Br (Br-10) was further investigated. ESR spectra was employed to identify the reactive species, whilst PL spectroscopy was performed to assess the charge separation for the photocatalysts. No signals corresponding to $\cdot O_2^-$ for both Br-10 and Br-40 were observed in the dark, whilst a strong signal corresponding to $\cdot O_2^-$ for Br-40 was observed under visible light irradiation in comparison to the $\cdot O_2^-$ signal for the Br-10 sample (Fig. 5c). This greater amount of $\cdot O_2^-$ generated for Br-40 compared to Br-10 directly correlates with the greater oxidation properties of Br-40. As more $\cdot O_2^-$ is produced, this generates more dissociative electrons and lowers the PL intensity. Lower PL intensities correspond to a lower recombination rate of electron-hole pairs, as well as higher charge separation efficiencies. As shown in Fig. 5d, Br-40 has the lowest PL intensity in contrast with the other samples, and hence displays the most excellent charge separation efficiencies.

The infrared spectra of the adsorption of NO and the corresponding photocatalytic NO oxidation under visible light irradiation by Br-10 and Br-40 is shown in Fig. S7 (Supporting informa-

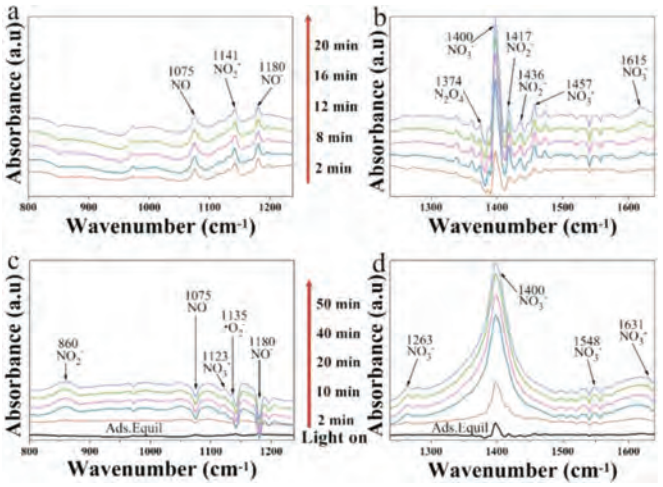

Fig. 6. *In situ* FT-IR spectra of the adsorption process of $NO + O_2$ for Br-40 (a, b). *In situ* FT-IR spectra of the reaction process of $NO + O_2$ for Br-40 (c, d).

tion) and Fig. 6. Tables S2 and S3 (Supporting information) show the IR peaks investigated during NO adsorption and oxidation by Br-10 and Br-40, respectively. The adsorption bands include 1075 cm^{-1}, 1180 cm^{-1}, 1374 cm^{-1} correspond to NO, NO^-, N_2O_4 were observed both on Br-10 and Br-40 due to physical adsorption of NO (Figs. S7a and b and Figs. 6a and b) [43–45]. NO appears to be oxidized by the surface-active radicals during the adsorption process. With increasing of adsorption time, the characteristic peaks corresponding to linear nitrite (1417 cm^{-1}) [46] and monodentate nitrates (1400 cm^{-1}) [47] were detected on Br-40, whilst weaker signals were observed in the presence of Br-10. Furthermore, an additional bidentate nitrites peak at 1615 cm^{-1} [46,48] was observed for the Br-10 sample and a depressing nitrite peak at 846 cm^{-1} [44] was also apparent over time. Other peaks corresponding to nitrites (1141 cm^{-1} and 1436 cm^{-1}) and nitrate (1457 cm^{-1}) were also detected in the presence of both Br-10 (Figs. S7a and S7b) and Br-40 (Figs. 6a and b) [46,48,49]. It appears more nitrites and nitrates are generated in the presence of Br-40 compared to Br-10 during adsorption.

As shown in Fig. S7c and Fig. 6c, visible light drives the photocatalytic oxidation of NO, and a signal corresponding to the surface superoxide species ($\cdot O_2^-$) at 1135 cm^{-1} increases with increase irradiation in the presence of both Br-10 and Br-40 (Eq. 3) [50]. The IR peaks corresponding to $\cdot O_2^-$ in the presence of Br-40 are more intense than that for Br-10, which is consistent with the ESR studies. IR spectroscopy, ESR, and PL studies indicate that the photocatalytic conversion of NO during visible light irradiation due to the action of surface $\cdot O_2^-$ radicals. In contrast with the adsorption process demonstrated in Figs. S7a and b and Figs. 6a and b, the bands corresponding to NO (1075 cm^{-1}) and NO^- (1180 cm^{-1}) gradually reduce, and the signal corresponding to N_2O_4 (1374 cm^{-1}) is not apparent after illumination (Figs. S7c-S7d and Figs. 6c and d). These results indicate NO, NO^- and N_2O_4 are consumed, while the peaks corresponding to nitrites (NO_2^-) at around 846 cm^{-1} on Br-10 appears. While for the Br-40 sample, a peak at 860 cm^{-1} corresponding to chelated nitrites (NO_2^-) was observed [44,49,51]. The proposed reactions are displayed in Eqs. 4–6. A large monodentate nitrates peak at 1400 cm^{-1} [47] significantly increased with increased of illumination time in the presence of both Br-10 and Br-40, where the nitrate peak was stronger on Br-40 compared to Br-10, which indicates Br-40 has a better NO removal activity. Several signals at 1548 cm^{-1}, 1123 cm^{-1}, and 1631 cm^{-1} corresponding to NO_3^- were also observed in the presence of both Br-10 and Br-40. Furthermore, in the presence of Br-10 a monodentate nitrates peak at 1281 cm^{-1} was observed. Whereas in the presence of Br-40, a band at 1263 cm^{-1} corresponding to bridging bidentate nitrates was apparent [46]. The intermediate reaction products appear to be oxidized by the abundant surface active radicals which avoids the accumulation of toxic products. Accordingly, more nitrates are produced in the presence of Br-40 than Br-10 under visible light irradiation, which is consistent with the photocatalytic activity result. Relevant formulas are displayed in Eqs. 7–10, shown below:

$$e^- + O_2(g) \rightarrow \cdot O_2^- \quad (3)$$

$$e^- + NO \rightarrow NO^- \quad (4)$$

$$NO + \cdot O_2^- \rightarrow NO_2^- + {}^*O \quad (5)$$

$$2NO^- + N_2O_4 \rightarrow 2NO_2^- + 2NO \quad (6)$$

$$NO + \cdot O_2^- \rightarrow NO_3^- \quad (7)$$

$$NO^- + \cdot O_2^- \rightarrow NO_3^- \quad (8)$$

$$NO_2^- + \cdot O_2^- \rightarrow NO_3^- + {}^*O \quad (9)$$

$$N_2O_4 + 2\cdot O_2^- \rightarrow 2NO_3^- + O_2 \quad (10)$$

In conclusion, we prepared a series of Br self-doped Bi_5O_7Br photocatalysts by a facile simple precipitation approach for the photocatalytic removal NO. In contrast with pristine Bi_5O_7Br, the optimal Br self-doping sample (Br-40) possessed excellent light adsorption, and high specific surface areas and pore volumes. DFT studies revealed the superior band structure, and strong interaction between NO and Br self-doped Bi_5O_7Br. Furthermore, the adsorption energy and transfer electron number for Br self-doped Bi_5O_7Br was more than three times that of Bi_5O_7Br for NO. Br-40 demonstrated the highest photocatalytic NO degradation performance due to superior superoxide radical generation and excellent charge separation. The intermediate products and reaction pathway for the photocatalytic oxidation of NO on Br-40 was determined by *in situ* DRIFT. The NO^- species is a crucial intermediate product involved in the conversion of NO into nitrate, which avoids the production of toxic by-products. Our investigation has furthered the understanding of the mechanisms surrounding photocatalytic NO removal, and revealed a highly active visible light photocatalyst for environmental purification.

Declaration of competing interest

There are no conflicts to declare.

Acknowledgments

This work was supported by the National Key Research and Development Program of China (No. 2019YFC0214404), Science and Technology Major Projects in Sichuan Province (No. 2019KJT0067–2018SZDZX0019), and Science and Technology Major Projects in Chengdu (No. 2018-ZM01–00044-SN). The authors also acknowledge AM-HPC in Suzhou, China for computational support.

Supplementary materials

Supplementary material associated with this article can be found, in the online version, at doi:10.1016/j.cclet.2021.10.082.

References

[1] X. Shi, P. Wang, W. Li, et al., Appl. Catal. B: Environ. 243 (2019) 322–329.
[2] H. Wang, Z. Qu, S. Dong, H. Xie, C. Tang, Environ. Sci. Technol. 50 (2016) 13511–13519.
[3] X. Li, G. Dong, F. Guo, et al., Environ. Sci. Nano 7 (2020) 1990–1998.
[4] C. Yuan, W. Cui, Y. Sun, et al., Chin. Chem. Lett. 31 (2020) 751–754.
[5] Y. Huang, Y. Yu, Y. Yu, B. Zhang, Solar RRL 4 (2020) 2000037.
[6] Y. Nosaka, A.Y. Nosaka, Chem. Rev. 117 (2017) 11302–11336.
[7] D. Ni, Y. Zhang, Y. Shen, S. Liu, Y. Zhang, Chin. Chem. Lett. 31 (2020) 115–118.
[8] L. Liu, H. Huang, Z. Chen, et al., Angew. Chem. Int. Ed. 60 (2021) 18303–18308.
[9] H. Wang, W. He, X.A. Dong, H. Wang, F. Dong, Sci. Bull. 63 (2018) 117–125.
[10] W. Cui, J. Li, F. Dong, et al., Environ. Sci. Technol. 51 (2017) 10682–10690.
[11] X. Xie, Q.U. Hassan, H. Lu, et al., Chin. Chem. Lett. 32 (2021) 2038–2042.
[12] X. Jin, L. Ye, H. Xie, G. Chen, Coordin. Chem. Rev. 349 (2017) 84–101.
[13] X. Meng, Z. Zhang, J. Mole. Catal. A: Chem. 423 (2016) 533–549.
[14] F. Dong, Y. Sun, M. Fu, Z. Wu, S.C. Lee, J Hazard. Mater. 219-220 (2012) 26–34.
[15] D. Mao, J. Yuan, X. Qu, et al., J. Catal. 369 (2019) 209–221.
[16] X. Jin, C. Lv, X. Zhou, et al., ChemSusChem 12 (2019) 2740–2747.
[17] Y. Liu, Z. Jiang, X. Zhang, P.K. Shen, J. Mater. Chem. A 6 (2018) 20037–20043.
[18] M. Ji, J. Di, Y. Liu, et al., Appl. Catal. B: Environ. 268 (2019) 118403.
[19] Y. Su, C. Ding, Y. Dang, et al., Appl. Surf. Sci. 346 (2015) 311–316.
[20] H. Xu, Y. Hu, D. Huang, et al., ACS Sustain. Chem. Eng. 7 (2019) 5784–5791.
[21] P. Li, Z. Zhou, Q. Wang, et al., J. Am. Chem. Soc. 142 (2020) 12430–12439.
[22] H. Yu, F. Chen, X. Li, et al., Nat. Commun. 12 (2021) 4594.
[23] T. Soltani, B.K. Lee, J. Hazard. Mater. 316 (2016) 122–133.
[24] F. Wang, D. Chen, N. Zhang, et al., J. Colloid. Interf. Sci. 508 (2017) 237–247.
[25] L. Zhang, X. Yue, J. Liu, et al., Sep. Purif. Technol. 231 (2020) 115917.
[26] Z. Jiang, G. Dong, R. Wang, et al., Solar RRL 4 (2020) 2000303.
[27] S. Wang, X. Han, Y. Zhang, et al., Small Struct. 2 (2020) 2000061.
[28] S. Wang, X. Hai, X. Ding, et al., Adv. Mater. 29 (2017) 1701774.
[29] M. Guan, C. Xiao, J. Zhang, et al., J. Am. Chem. Soc. 135 (2013) 10411–10417.
[30] Z. Zhao, X. Wang, Z. Shu, et al., Appl. Surf. Sci. 455 (2018) 591–598.
[31] J. Wang, S. Su, B. Liu, M. Cao, C. Hu, Chem Commun 49 (2013) 7830–7832.
[32] M. Kulbak, I. Levine, E. Barak-Kulbak, et al., Adv. Energy Mater. 8 (2018).
[33] H. Wang, X.a. Dong, R. Tang, et al., Appl. Catal. B: Environ. 277 (2020) 119214.
[34] X. Ding, K. Zhao, L. Zhang, Environ. Sci. Technol. 48 (2014) 5823–5831.
[35] J.F.G. Kresse, Comp. Mater. Sci. 6 (1996) 15–50.
[36] J.F.G. Kresse, Phys. Rev. B 54 (1996) 11169–11180.
[37] K.B. John, P. Perdew, Matthias Ernzerhof, Phys. Rev. Lett. 77 (1996) 3865–3868.
[38] D.J.G. Kresse, Rhys. Rev. B 59 (1999) 1758–1775.
[39] P.E. Blochl, Phys. Rev. B 50 (1994) 17953–17979.
[40] H. Li, T. Hu, N. Du, et al., Appl. Catal. B: Environ. 187 (2016) 342–349.
[41] X.a. Dong, W. Zhang, Y. Sun, et al., J. Catal. 357 (2018) 41–50.
[42] H. Wu, C. Yuan, R. Chen, et al., ACS Appl. Mater. Interfaces 12 (2020) 43741–43749.
[43] Y. Lv, C. Pan, X. Ma, et al., Appl. Catal. B: Environ. 138-139 (2013) 26–32.
[44] B. Lei, W. Cui, J. Sheng, et al., Sci. Bull. 65 (2020) 467–476.
[45] L. Sivachandiran, F. Thevenet, A. Rousseau, D. Bianchi, Appl. Catal. B: Environ. 198 (2016) 411–419.
[46] C. Sedlmair, J. Catal. 214 (2003) 308–316.
[47] X. Wang, Y. Yu, H. He, Appl. Catal. B: Environ. 100 (2010) 19–30.
[48] M. Kantcheva, J. Catal. 223 (2004) 352–363.
[49] J. Wu, Y. Cheng, J. Catal. 237 (2006) 393–404.
[50] H. Shang, S. Huang, H. Li, et al., Chem. Eng. J. 386 (2020) 124047.
[51] W. Cui, J. Li, W. Cen, et al., J. Catal. 352 (2017) 351–360.